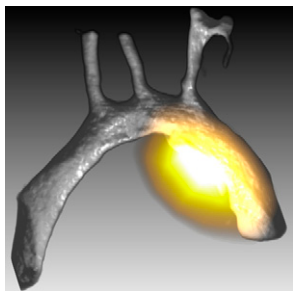


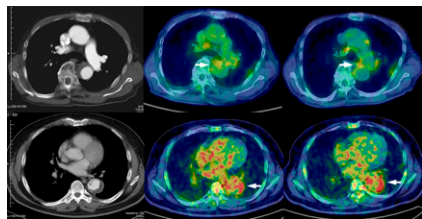
Imaging of MMP activity in plaques: Schäfers and colleagues review the rationale, potential, and current status of matrix-metalloproteinases in the clinical context of stroke and myocardial infarction. *Page 663*



Cardiac PET: Rudd provides perspective on the clinical appearance of acute aortic dissection and previews 2 articles in this issue of *JNM* on the utility of PET in predicting adverse outcomes. . . *Page 667*

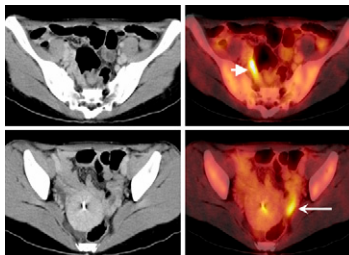
⁶⁸Ga-DOTATOC PET/CT and NETs: Ambrosini and colleagues retrospectively assess the effect of ⁶⁸Ga-DOTA-peptide PET/CT on staging and clinical management of patients with neuroendocrine tumors. *Page 669*

Aortic dissection and PET/CT: Kato and colleagues investigate the use of ¹⁸F-FDG PET/CT to predict short- and midterm outcomes, including progression and increased risk of rupture, in patients with medically controlled acute aortic dissection. *Page 674*

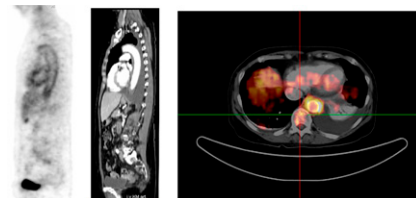


Bilateral pelvic ¹⁸F-FDG uptake: Yun and colleagues report on fallopian tube tracer uptake in premenopausal women at mid-menstrual cycle and discuss the re-

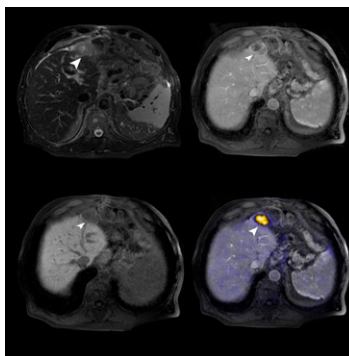
lationship of these findings to the presence and influence of estrogen. *Page 682*



Acute vs. chronic aortic dissection: Reeps and colleagues use ¹⁸F-FDG PET/CT to analyze aortic wall uptake differences in acute and chronic stable aortic dissection and point to the potential for clinical application of this technique. *Page 686*

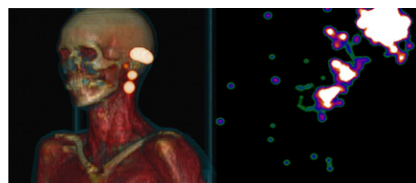


Fused PET-MRI and liver lesions: Donati and colleagues compare the accuracy of lesion detection and diagnostic confidence among ¹⁸F-FDG PET/CT, gadolinium-enhanced MRI, and retrospectively fused PET and MR images in suspected liver metastases. *Page 692*

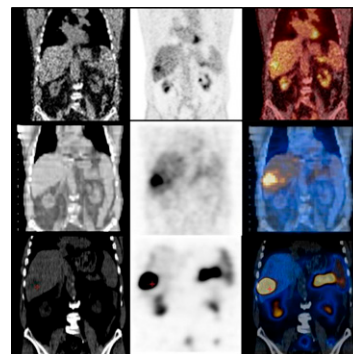


Intraoperative sentinel node imaging: Vermeeren and colleagues introduce and evaluate a portable γ -camera for intraoperative

visualization of sentinel nodes in the head and neck region. *Page 700*



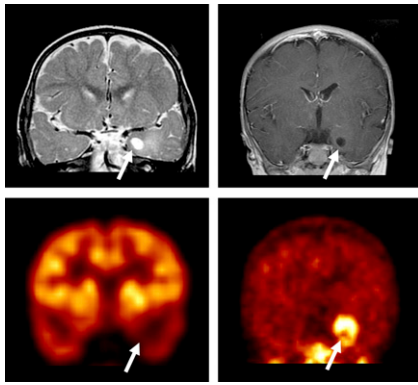
Optimal NET imaging: Binderup and colleagues compare ¹¹¹In-DTPA-octreotide somatostatin receptor scintigraphy, scintigraphy with ¹²³I-MIBG, and ¹⁸F-FDG PET in patients with histologically verified neuroendocrine tumors. *Page 704*



¹⁸F-FLT PET in oral cavity tumors: Troost and colleagues report on validation studies on the effectiveness of ¹⁸F-fluorothymidine as a PET tracer in noninvasive assessment of the proliferative state of squamous cell carcinomas of the oral cavity. *Page 713*

¹⁸F-FLT kinetics in brain tumor treatment: Schiepers and colleagues detail the kinetics of ¹⁸F-fluorothymidine during treatment of malignant glioma with bevacizumab and irinotecan and describe the tracer's potential as a biomarker of cell proliferation. *Page 720*

¹⁸F-FDG and ¹¹C-methionine PET in epilepsy: Phi and colleagues compare these 2 tracers in PET evaluation of children with focal cortical dysplasia and mixed neuronal and glial tumors, where presurgical MRI may be indeterminate. *Page 728*



Radioaerosol choice in V/Q SPECT: Jögi and colleagues compare ^{99m}Tc -DTPA and Technegas in ventilation-perfusion SPECT studies in patients with and without obstructive lung disease. **Page 735**

Assessing liver function: de Graaf and colleagues provide an educational overview of nuclear imaging techniques, including biochemical and technical backgrounds, for assessment of hepatic function in liver surgery and transplantation. **Page 742**

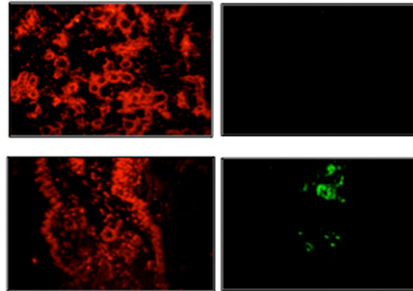
Biased PET images: Son and colleagues look at challenges in PET scanners with elongated fields of view and explore the effects of and remedies for inaccurate attenuation coefficients. **Page 753**

Monitoring antiangiogenic response: Nagengast and colleagues study ^{89}Zr -bevacizumab PET for early antiangiogenic tumor response evaluation after treatment with the new heat shock protein 90 inhibitor NVP-AUY922. **Page 761**

Folate targeting in atherosclerosis: Ayala-López and colleagues examine the use of a folate-targeted ^{99m}Tc -labeled chelate for imaging macrophages that accumulate in atherosclerotic plaques, internalize cholesterol-

rich lipoprotein particles, and evolve into foam cells to form vulnerable atherosclerotic lesions. **Page 768**

Annexin V for apoptosis in breast cancer: Erba and colleagues use ^{99m}Tc -annexin V scintigraphy to define the time course of apoptosis induced by paclitaxel in a model of virus-induced murine breast cancer. **Page 775**



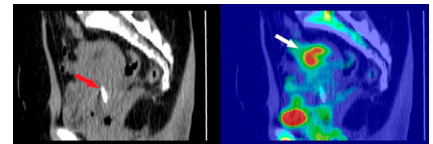
Nanobodies for immune cell imaging: De Groeve and colleagues explore the use of nanobodies as a generic method for imaging in vivo biodistribution of specific immune cell types, with myeloid cells as an example. **Page 782**

PET tracers in brain hematoma: Salber and colleagues compare patterns and time courses of ^{18}F -FET and ^3H -MET uptake in PET imaging of rats with cerebral hematomas and discuss challenges in differentiating between neoplastic and nonneoplastic hematoma origins. **Page 790**

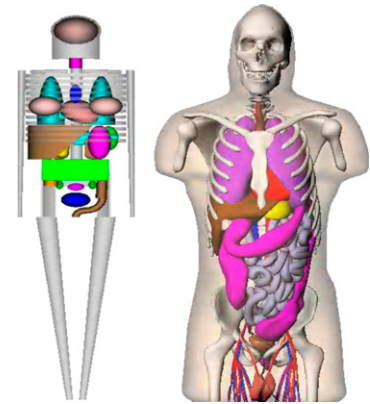
^{11}C -choline in atherosclerosis imaging: Laitinen and colleagues investigate the feasibility of ^{11}C -choline as a PET tracer in the assessment of degree of inflammation in atherosclerotic plaques in an atherosclerotic mouse model. **Page 798**

^{18}F -FDG fetal dosimetry: Zanotti-Fregonara and colleagues calculate the total fetal absorbed

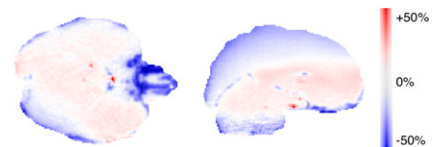
dose in a rare case of ^{18}F -FDG PET/CT imaging in early pregnancy. **Page 803**



Radiation dose variation with stature: Marine and colleagues assess variations in specific absorbed energy fractions in adults with different sizes but normal body stature. **Page 806**



PET/MRI attenuation correction: Keereman and colleagues describe MRI-based attenuation correction for PET/MRI using ultrashort echo time sequences. **Page 812**



ON THE COVER

In a study exploring the feasibility of using ^{11}C -choline to assess inflammation in atherosclerotic plaques, high ^{11}C -choline uptake was found in the aortic plaques of atherosclerotic mice. Data suggest that macrophages may be responsible for the uptake.

See page 800.

